DYNAMICS AND COLLISION OF NON-SPHERICAL ELLIPSOID PARTICLES IN TURBULENT CHANNEL FLOW

Connor NOLAN[1], Lee MORTIMER[2], Peter JIMACK[3], Michael FAIRWEATHER[4]

[1] Corresponding Author. EPSRC Centre for Doctoral Training in Future Fluid Dynamics, Faculty of Engineering and Physical Sciences, University of Leeds. Leeds LS2 9JT, United Kingdom. E-mail: mm18cn@leeds.ac.uk

[2] School of Chemical and Process Engineering, Faculty of Engineering and Physical Sciences, University of Leeds. Leeds LS2 9JT, United Kingdom. E-mail: l.f.mortimer@leeds.ac.uk

[4] School of Computer Science, Faculty of Engineering and Physical Sciences, University of Leeds. Leeds LS2 9JT, United Kingdom. E-mail: p.k.jimack@leeds.ac.uk

[4] School of Chemical and Process Engineering, Faculty of Engineering and Physical Sciences, University of Leeds. Leeds LS2 9JT, United Kingdom. E-mail: m.fairweather@leeds.ac.uk

ABSTRACT

Non-spherical particle-laden flows in pipes and channels are of importance in numerous industrial, environmental, and biological processes, making their study essential for understanding and optimising particle transport, deposition, and interaction dynamics. In this work the spatial and orientational dynamics of rigid ellipsoidal particles in turbulent channel flow are explored. A high-fidelity spectral element method-based direct numerical simulation is employed to solve for the fluid phase which is coupled to a Lagrangian particle tracker for modelling the dispersed particles. Particle translational motion is governed by inertia, hydrodynamic lift, and drag, while their rotational dynamics is described by the Euler equations of rotation, accounting for external hydrodynamic torques. Quaternions are utilised to track particle orientations over time. Full four-way coupling between the particles and the fluid is implemented, capturing both the influence of the fluid on the particles and the feedback effect of the particles on the continuous phase. The latter is modelled using a local element-based force feedback field in the Navier-Stokes equations. Particle-particle collisions are also resolved. The fluid and particle phases are validated across multiple particle aspect ratios, Reynolds and Stokes numbers with emphasis on reproducing spatial and orientational dynamics consistent with the literature. Fully coupled simulations are then conducted to evaluate collision statistics across all regions of the channel with results being compared to those of spherical particles to elucidate the underpinning micro-scale dynamics present in such flows as well as providing avenues for further research.

Keywords: Collision dynamics, non-spherical particles, turbulent channel flow, Lagrangian particle tracker, four-way coupling

NOMENCLATURE

$\underline{A}$	[-]	rotation matrix
A_D	[m^2]	projected area normal to drag
A_L	[m^2]	projected area normal to lift
C_D	[-]	drag coefficient
C_L	[-]	lift coefficient
F_D	[m/s^2]	drag force
F_L	[m/s^2]	lift force
F_{PG}	[m/s^2]	pressure gradient force on particle
F_{VM}	[m/s^2]	virtual mass force
$\underline{\underline{G}}$	[s^{-1}]	velocity gradient matrix
f_{PG}	[m/s^2]	pressure gradient force on fluid
f_{2W}	[m/s^2]	particle force feedback source term
q	[-]	quaternion vector
u_s	[m/s]	slip-velocity
z'	[-]	direction of principal particle axis
Ω	[s^{-1}]	angular velocity
α	[-]	angle of incidence
δ	[m]	half channel height
λ	[-]	aspect ratio
ρ^*	[-]	density ratio
ϕ_p	[-]	volume fraction

Subscripts and Superscripts

p, F	particle, fluid
L, D	lift, drag
PG, VM	pressure gradient, virtual mass
B, τ	bulk, shear
*	non-dimensional units (bulk scales)

1. INTRODUCTION

Particle-laden flows are ubiquitous in nature and industry, such as in the formation of riverbeds [1] and the transportation of nuclear waste [2]. In such flows the collision of small, heavy, non-spherical particles occurs frequently, for example in papermaking [3] and in clouds [4]. Understanding both the particle-scale and bulk-scale dynamics in such flows is of importance to be able to effectively predict long-scale phenomena such as deposition, turbulence modulation and blockages. This knowledge allows for the optimisation of processes and ensures the effectiveness and safety of new systems.

In recent years advances in computational performance, direct numerical simulation and Lagrangian particle tracking methodologies have aided the prediction of particle-laden flows at scales relevant to those seen in industry. These models have reproduced many of the bulk-scale dynamics noted in the literature such as turbophoresis and preferential concentration [5]. The development and optimisation of computational fluid dynamics (CFD) has led to these methods surpassing the resolution of experimental methodologies in the study of particle scale interactions. This means that for reliable results first-principles techniques with proven high accuracy, for example direct numerical simulation (DNS) which can resolve relevant length, and time scales down to the Kolmogorov scale [6], currently provide the only means of assessing certain phenomena.

Significant contributions have been made in the study of spherical particle-laden turbulent flows at low-volume fractions ($\phi_p \leq 10^{-6}$) where only the effect of the fluid on the particles is considered in so called one-way coupled simulations. These studies elucidate the mechanisms underpinning particle migration such as preferential concentration and turbophoresis. Preferential concentration is seen most strongly at low Stokes numbers where particle clustering in low-velocity streaks and the near-wall region is noted [7]. Turbophoresis describes the tendency of particles to move towards areas with lower-than-average turbulence kinetic energy and has been shown to scale with the particle Stokes number [8]. The interaction between particles and turbulent structures in the near-wall region has been studied in detail with a wide range of behaviours being noted based upon the material and inertial properties of the system [9]. The dynamics, both translational and rotational, of non-spherical ellipsoidal particles has also been studied using one-way coupled Lagrangian particle tracking (LPT) simulations. Most of the studies on this topic examine prolate ellipsoids with aspect ratios $\lambda > 1$, often referred to in the literature as fibres. It was found that the aspect ratio has little effect on particle clustering, preferential concentration or segregation [10]. An analysis of near-wall dynamics showed that orientational and translational behaviours influence accumulation at the wall with longer fibres being deposited at higher rates. Moreover, it was noted that fibres tend to align with the mean streamwise flow direction near the wall with this alignment being increasingly unstable for higher particle inertia. Complex behaviour is observed in the spanwise and wall-normal directions due to fibre inertia and elongation, with no preferential orientation or significant segregation observed in the channel centre where the turbulent conditions are close to isotropic.

As volume fraction increases ($10^{-6} \leq \phi_p \leq 10^{-3}$) it becomes necessary to account for the impact of the particles back onto the fluid in so-called two-way coupling. This is typically done using the method of particle force feedback on the turbulent fluid phase [11]. Various studies in wall-bounded turbulence found that large particles enhance turbulence while small particles dampen it, and interestingly it has been shown that this effect is muted at low density ratios even when the particle Stokes number is equivalent in each case. In the case of large particle Stokes numbers, the particles have more inertia and are thus less responsive to rapid changes in the local flow, resulting in preferential accumulation in low turbulence regions. This leads to local turbulence attenuation or suppression hindering the energy transfer across turbulence scales [6].

As the volume fraction increases further to around $\phi_p > 10^{-3}$, the translational and rotational motion of the particle begins to be affected by inter-particle collisions which at this point occur very frequently. It is therefore necessary for simulations to be able to detect and resolve such collisions which is computationally expensive, especially in the case of non-spherical particles. Collision-driven turbulent particle-laden flows have been studied extensively, and in one study low Stokes number particle were found to accumulate in regions of irrotational dissipation due to vortex ejection. The authors also noted a relationship between the relative collision velocity and Reynolds number, especially in the case of low Stokes number particles [12]. Work performed simulating a particle-laden vertical channel using a four-way coupled LPT showed that micro particles can modify the fluid turbulence statistics even at very low volume fractions of the order $\phi_p \approx 10^{-5}$ because of the quantity of collisions [13]. Four-way coupling has been applied alongside particle non-sphericity within an LPT but there is little literature quantifying the effect of particle shape on collision dynamics. One study investigated the settling of ellipsoidal particles within isotropic turbulence, finding that ellipsoids collide considerably more often than spherical particles of the same volume and in these collisions the relative velocity was higher [14]. Another study focusing on the collision and coupling effects of high

inertia particles was conducted in [5], revealing that high speed particle collisions lead to larger momentum transfer and directional redistribution, which increases the magnitude and changes the direction of the slip velocity. This study noted the importance of four-way coupling when simulating midrange Stokes numbers.

Various collision detection methods have been developed including nearest-neighbour lists and stochastic models. In this study we use a deterministic partition-based method [15] for collision detection. Post collision calculations are conducted using a hard-sphere model. More sophisticated collision detection algorithms for non-spherical particles have been proposed where the particle volume is approximated by a collection of overlapping fictitious spheres of varying radii [16]. This representation allows for similar contact procedures as those mentioned above for the case of spheres.

The present study aims to advance the understanding of collision dynamics in wall-bounded particle-laden turbulent channel flow, with a focus on the impacts of particle non-sphericity and high inertia. We seek to provide deeper insights into these complex interactions and to generate collision conditions typical of those seen in channels of industrial interest.

2. METHODOLOGY

2.1. Fluid Phase Modelling

To generate accurate predictions of the flow field we utilise the spectral element method-based DNS code Nek5000 [17] to fully resolve all relevant length and time scales. The solver employs an order seven spectral method on each element. We simulate a turbulent channel flow at shear Reynolds number $Re_\tau = u_\tau \delta / \nu_F = 300$, where u_τ is the shear velocity, δ is the half channel height and ν_F is the fluid kinematic viscosity. The reasons for using Nek5000 are twofold, firstly the open-source nature of the solver makes it suitable for modification and extension, secondly the code comes with efficient parallelisation and an extensive history of validation making it an efficient and safe choice. The governing equations for the continuous phase dynamics are the incompressible Navier-Stokes equations, which are given in dimensionless form as follows:

$$\nabla \cdot \boldsymbol{u}_F^* = 0, \tag{1}$$

$$\frac{D\boldsymbol{u}_F^*}{Dt^*} = -\nabla p^* + \frac{1}{Re_B}\nabla^2 \boldsymbol{u}_F^* + \boldsymbol{f}_{PG}^* + \boldsymbol{f}_{2W}^*, \tag{2}$$

where $\boldsymbol{u}_F^*(\boldsymbol{x}^*, t^*)$ is the fluid velocity vector at position $\boldsymbol{x}^*$ and time t^*, $p^*(\boldsymbol{x}^*, t^*)$ is the fluid pressure, $Re_B = u_B \delta / \nu_F$ is the bulk Reynolds number, $\boldsymbol{f}_{PG}^*$ is the constant pressure gradient forcing term and $\boldsymbol{f}_{2W}^*$

is an arbitrary cell-dependent forcing term accounting for two-way momentum exchange between particles and fluid. Parameters marked with an asterisk (∗) signify a non-dimensional variable obtained from the bulk properties (δ, u_B, ρ_F) where ρ_F is the density of the fluid. These governing equations are solved on a discretised, structured grid which consists of $27 \times 18 \times 23$ seventh-order spectral elements, equivalent to 3.9 M nodes. Mesh refinement is used in the wall-normal direction, while the distribution of elements is uniform in the streamwise and spanwise directions. For our simulation (x, y, z) correspond to the streamwise, wall-normal and spanwise directions respectively. The simulation domain and corresponding mesh are illustrated in Figure 1.
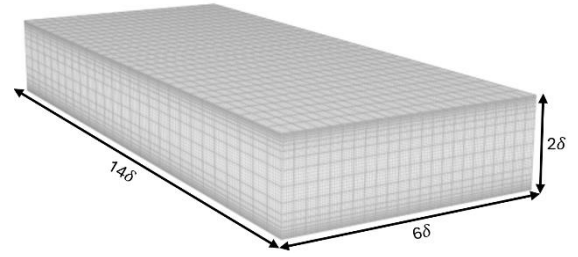
Figure 1. Computational mesh demonstrating element spacings and increased near-wall nodal density

The solver uses a constant time step of $\Delta t^* = 0.0025$. Periodic conditions are imposed in the streamwise and spanwise directions to ensure that the flow remains cyclic. The top and bottom walls at $y^* = \pm 1$ respectively are subject to no-slip and impermeability conditions. The flow is driven by a constant pressure gradient, chosen to obtain a specific Reynolds number, applied in the streamwise direction, the magnitude of which is given as follows:

$$\frac{dp^*}{dx^*} = \left(\frac{Re_\tau}{Re_B}\right)^2. \tag{3}$$

2.2. Lagrangian Particle Tracking

For the tracking of particle trajectories and orientations through the flow, a Lagrangian particle tracking code has been developed to run in parallel with Nek5000. Each particle is represented as a point with its location, velocity, quaternions and angular velocity being updated each time-step by solving a set of dimensionless equations. The equations for the linear motion are derived through considering the balance between the particle's inertia and the fluid. We consider the effects of the following forces: lift, drag, virtual mass and the pressure gradient. The Basset history force is neglected due to its limited impact relative to its computational cost, also neglected are the effects of gravity and buoyancy to allow us to more easily

isolate the effect of the turbulence on the particles. For the rotational motion we use quaternions to track the orientation of the particles and update the angular velocity using Euler's equations of rotation. For these, we consider the torque due to the resistance on a rotating ellipsoid and the cross-coupling between angular velocities along different axes, which arises because the principal moments of inertia are not all the same.

In this work we consider non-spherical ellipsoid particles given by the equation:

$$\left(\frac{x'}{a}\right)^2 + \left(\frac{y'}{b}\right)^2 + \left(\frac{z'}{c}\right)^2 = 1, \qquad (4)$$

where a, b and c represent the lengths of the three semi-principal axes in the x', y' and z' directions respectively. We enforce that $a = b$ in all cases and define the aspect ratio $\lambda = c/a$. The solid phase can then be characterised by specifying the following bulk parameters: the particle density ρ_p, the aspect ratio and the volume fraction ϕ_p defined as follows,

$$\phi_p = \frac{4}{3}\pi a^2 c \frac{N_p}{V_F}, \qquad (5)$$

where N_p is the number of particles and V_F is the volume of the fluid geometry. The particle dynamics are modelled using three reference frames: the particle frame $x' = [x', y', z']$ with its origin at the particle's centroid and its principal axis z', the global (fixed) frame $x = [x, y, z]$ and the co-moving frame $x'' = [x'', y'', z'']$ which shares its origin with the particle centroid and has axes parallel to the fixed frame. Transformation between the co-moving frame and the particle frame can be performed as follows:

$$x' = \underline{\underline{A}}x'', \qquad (6)$$

Where $\underline{\underline{A}}$ is the time-dependent rotational matrix with elements expressed in terms of four quaternions $q = [q_0, q_1, q_2, q_3]^T$ satisfying the constraint $q_0^2 + q_1^2 + q_2^2 + q_3^2 = 1$.

The time evolution of the quaternions is used to update the orientation of the particles and is computed as:

$$\frac{dq}{dt^*} = \frac{1}{2}\begin{bmatrix} q_0 & -q_1 & -q_2 & -q_3 \\ q_1 & q_0 & -q_3 & q_2 \\ q_2 & q_3 & q_0 & -q_1 \\ q_3 & -q_2 & q_1 & q_0 \end{bmatrix}\begin{bmatrix} 0 \\ \Omega_{x'} \\ \Omega_{y'} \\ \Omega_{z'} \end{bmatrix}, \qquad (8)$$

where $\Omega_{x'}$, $\Omega_{y'}$ and $\Omega_{z'}$ are the components of the particle angular velocity expressed in the particle frame. The particle equations of motion and rotation are given below:

$$\frac{dx_p^*}{dt^*} = u_p^*, \qquad (9)$$

$$\frac{\partial u_p^*}{\partial t^*} = \frac{1}{M_{VM}}[F_D + F_L + F_{VM} + F_{PG}], \qquad (10)$$

where u_p^* denotes the dimensionless fluid velocity, $M_{VM} = (1 + 1/2\rho^*)$ is the dimensionless virtual mass factor where $\rho^* = \rho_p/\rho_F$ is the dimensionless density ratio. Here, F_D is the drag force acting on the particle and is given as follows [18]:

$$F_D = \frac{A_D^* C_D |u_s^*| u_s^*}{2\rho^* V_p^*}, \qquad (11)$$

where $V_p^* = (4/3)\pi a^{*2} c^*$ is the dimensionless volume of the particle, $u_s^* = u_F^* - u_p^*$ is the slip velocity, and A_D and A_L are the partial projected areas normal to the direction of the drag and lift forces respectively [18]:

$$A_D = \pi a^2 \sqrt{\cos^2(\alpha) + \left(\frac{4\lambda}{\pi}\right)^2 \sin^2(\alpha)}, \qquad (12)$$

$$A_L = \pi a^2 \sqrt{\sin^2(\alpha) + \left(\frac{4\lambda}{\pi}\right)^2 \cos^2(\alpha)}, \qquad (13)$$

where α is the angle of incidence defined as the angle between the slip velocity u_s^* and the direction of the principal particle axis z'. The dimensionless drag coefficient C_D for the non-spherical particles is given by [19]:

$$\frac{C_D}{K_2} = \frac{24}{Re_p K_1 K_2}\left[1 + 0.118\left(Re_p K_1 K_2\right)^{0.6567}\right] + \frac{0.4305}{1 + 3305/\left(Re_p K_1 K_2\right)}, \qquad (14)$$

where $Re_p = u_s^* d_{ev}/\nu_F$ is the particle Reynolds number computed using the equal volume sphere diameter $d_{ev} = 2a\lambda^{1/3}$, $K_1 = \frac{1}{3}(d_n/d_{ev} + 2\Phi_s^{-0.5})$ and $K_2 = 10^{1.8148(-\log\Phi_s)^{0.5743}}$ are the Stokes and Newton shape factors that model the particle sphericity and orientation, respectively, $d_n = \sqrt{4A_D/\pi}$ and $\Phi_s = s/S$, where Φ_s is the particle sphericity, defined as the ratio of the surface area of a sphere having the same volume as the particle, s, to the actual surface area of the non-spherical particle, S. The lift coefficient C_L is determined by the following [18]:

$$\frac{|C_L|}{|C_D|} = |\sin^2(\alpha)\cos^2(\alpha)|. \qquad (15)$$

The lift force F_L is therefore given by [18]:

$$F_L = \frac{1}{2\rho^* V_p^*}A_L^* C_L \frac{(z' \cdot u_s^*)}{|u_s^*|}[z' \times u_s^*] \times u_s^*. \qquad (16)$$

The local pressure gradient force F_{PG} is [5]:

$$F_{PG} = \frac{1}{\rho^*}\frac{Du_F^*}{Dt^*}. \qquad (17)$$

4

The virtual mass force $\boldsymbol{F}_{MV}$ is given by [5]:

$$\boldsymbol{F}_{VM} = \frac{1}{2\rho^*}\frac{D\boldsymbol{u}_F^*}{dt^*}. \tag{18}$$

The final equations of motion for the rotation of the prolate $(\lambda > 1)$ ellipsoid particles are given by Euler's equations of rotation presented below in a simplified dimensionless form [10] :

$$\frac{d\Omega_{x'}^*}{dt^*} = \frac{20[(1-\lambda^2)d_{z'y'}^* + (1+\lambda^2)(\omega_{z'y'}^{*'} - \Omega_{x'}^*)]}{Re_B(\beta_0 + \lambda^2\gamma_0)(1+\lambda^2)\rho^* a^{*2}}$$
$$+ \left(1 - \frac{2}{1+\lambda^2}\right)\Omega_{y'}^*\Omega_{z'}^*,$$

$$\frac{d\Omega_{y'}^*}{dt^*} = \frac{20[(\lambda^2-1)d_{x'z'}^* + (\lambda^2+1)(\omega_{x'z'}^{*'} - \Omega_{y'}^*)]}{Re_B(\alpha_0 + \lambda^2\gamma_0)(1+\lambda^2)\rho^* a^{*2}} \tag{19}$$
$$+ \left(\frac{2}{1+\lambda^2} - 1\right)\Omega_{x'}^*\Omega_{z'}^*,$$

$$\frac{d\Omega_{z'}^*}{dt^*} = \frac{20(\omega_{y'x'}^{*'} - \Omega_{z'}^*)}{Re_B(2\alpha_0)\rho^* a^{*2}}.$$

Here the elements of the deformation rate tensor $(d_{z'y'}$ and$d_{x'z'})$ and the spin tensor $(\omega_{z'y'}, \omega_{x'z'}$ and$\omega_{y'x'})$ are defined as follows:

$$d_{i'j'} = \frac{1}{2}\left(\frac{\partial u_{i'}}{\partial j'} + \frac{\partial u_{j'}}{\partial i'}\right),$$
$$\tag{20}$$
$$\omega_{z'y'} = \frac{1}{2}\left(\frac{\partial u_{i'}}{\partial j'} - \frac{\partial u_{j'}}{\partial i'}\right).$$

The velocity gradients in the particle frame $G_{i'j'}$ can be obtained by transforming the velocity gradients from the fixed frame$G_{ij} = \partial u_i/\partial x_j$:

$$G_{i'j'} = \underline{\underline{A}}\, G_{ij}\, \underline{\underline{A}}^{-1}. \tag{21}$$

The non-dimensional coefficients $\alpha_0 = \beta_0$, and γ_0 for a prolate ellipsoid $(\lambda > 1)$ are defined as [20]:

$$\alpha_0 = \frac{\lambda^2}{\lambda^2-1} + \frac{\lambda}{2(\lambda^2-1)^{3/2}}\ln\left(\frac{\lambda-\sqrt{\lambda^2-1}}{\lambda+\sqrt{\lambda^2-1}}\right),$$
$$\tag{22}$$
$$\gamma_0 = \frac{2}{\lambda^2-1} + \frac{\lambda}{(\lambda^2-1)^{3/2}}\ln\left(\frac{\lambda-\sqrt{\lambda^2-1}}{\lambda+\sqrt{\lambda^2-1}}\right).$$

The governing equations Eqs. (8) to (10) are integrated in time using a fourth-order Runge-Kutta (RK4) algorithm, while Eq. (19) is integrated using a mixed explicit/implicit differencing scheme presented in [20] due to the stiffness of the equations. In both cases the time-step is chosen to be the same as for the continuous phase solver.

For higher volume fractions, as considered in this work, it is essential to account for the particles' impact back onto the fluid and this is done by adding an additional source term in the Navier-Stokes equations. The acceleration applied to cell i is given by [11]:

$$\boldsymbol{f}_{2W}^{*i} = \frac{1}{V_i^*}\sum_j^{N_{p,i}}\frac{\partial\boldsymbol{u}_{p_j}^*}{\partial t^*}, \tag{23}$$

where $V_i^*$is the volume of the computational cell, and j is an index that iterates over the number of particles contained within a cell, $N_{p,i}$.

All inter-particle and wall collisions assume that the particles are spherical with radius equal to the largest semi-major axis. A deterministic binary collision search algorithm is also used, based on [21]. At each time-step, particles are distributed into cells of a coarse mesh. The collision algorithm detects collisions by comparing relative displacements and velocities within each cell. A secondary search identifies missed collisions. Collisions are resolved using kinetic energy and momentum conservation, with particles deflected to account for penetration. Collisions are assumed fully elastic.

3. RESULTS AND DISCUSSION

Here we focus on the collision dynamics of needle-like particles and compare our findings to those of nearly spherical particles. The fixed particle phase parameters have been chosen to match those of the study [5] and are shown in Table 1. Two particle shapes are considered, and the case specific parameters are outlined in Table 2. Here $St^+ = (\rho^* d_{ev}^{+2})/18\nu_F$ is the dimensionless shear Stokes number where $d_{ev} = 4a\lambda^{1/3}$.

Table 1. Fixed simulation parameters

Fixed Parameter	Value
Number of Particles N_p	300,000
Particle Volume V_p^*	6.55×10^{-4}
Volume Fraction ϕ_p	1.4×10^{-4}
Shear Stokes Number St^+	50
Density Ratio ρ^*	400
Shear Reynolds Number Re_τ	300
Bulk Reynolds Number Re_B	4,900

Table 2. Case specific particle phase parameters

| Case	a^*	c^*	λ
Near-Spheres	0.002492	0.002517	1.01
Needles	0.001462	0.007310	5

The particles were injected into the domain with random initial position and orientation. The initial velocity was inherited from the fluid and the initial angular velocity was set to zero. Our analysis breaks the flows into four distinct regions where the flow conditions are known to differ, namely the viscous sublayer (VS) $(0.973 < |y*| \leq 1)$, the buffer layer (BL) $(0.834 < |y*| \leq 0.973)$, the log-law region (LL) $(0.8 < |y*| \leq 0.834)$ and the bulk flow (BF) $(0 \leq |y*| \leq 0.8)$. We quantify the

5

alignment of particles by considering the cosine of the angles $(\theta_x, \theta_y, \theta_z)$ made between the axes of co-moving frame x'' and the principal particle axis z'. These are known as the direction cosines denoted $\cos(\theta_i)$. Values $\cos(\theta_i) \approx 1$ indicate the fibre is aligned strongly with axis i, while $\cos(\theta_i) \approx 0$ indicate the fibre is unaligned with axis i. The following PDFs are calculated using a Gaussian kernel density estimation.
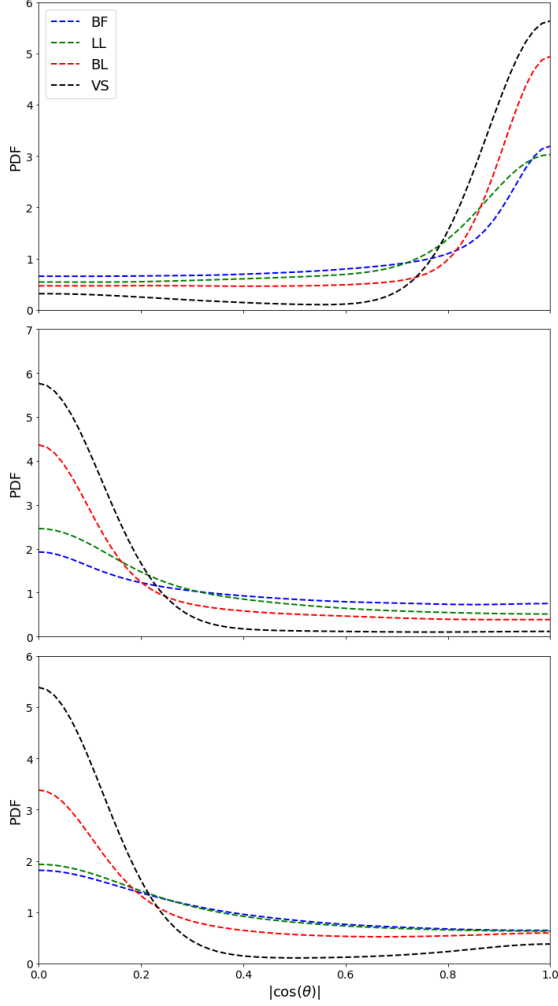

Figure 2: Absolute direction cosine PDFs by wall normal location for needle-like particles, (top) streamwise alignment, (middle) wall normal alignment and (bottom) spanwise alignment

The alignment of the needle-like particles is quantified in Figure 2. We see strong alignment with the streamwise direction close to the wall with the alignment weakening towards the centre of the channel. The spanwise and wall-normal directions behave similarly with strong anti-alignment with the respective axes close to the walls which again weakens toward the channel centre. These findings are consistent with previous studies investigating needle-like particles [10], thus providing validation of the orientational dynamics of the model.
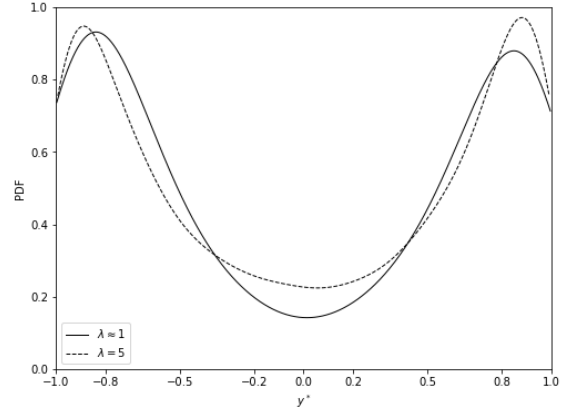
**Figure 3: Collision PDFs by wall normal location**
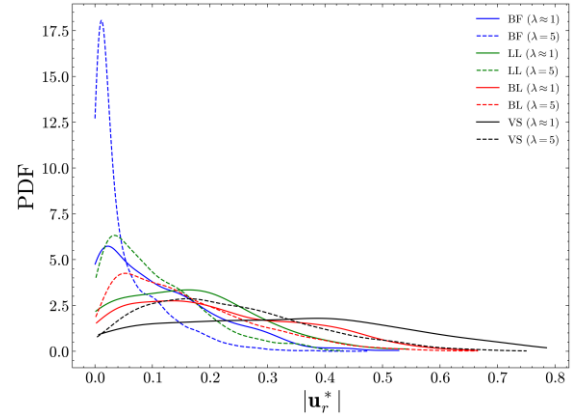
Figure 4: Collided particle absolute relative velocity PDFs separated by flow region
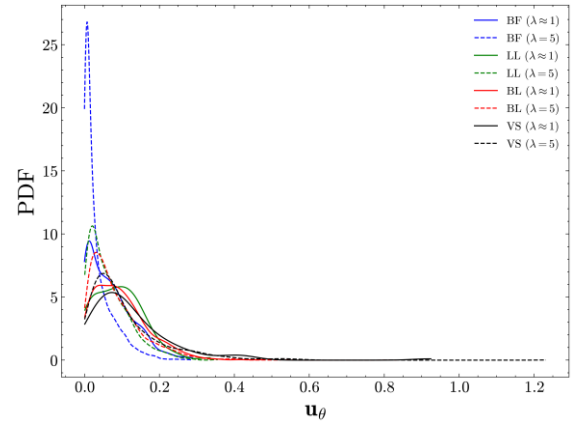

Figure 5: Collided particle relative collision angle (radians) PDFs separated by flow region

We observe that both the near-spheres and needles collide more often closer to the walls, likely due to turbophoresis within the channel leading to preferential concentration in the near wall region (see Figure 3). The needles collide with a higher probability in the very near wall region but the distribution falls more quickly as we move from the wall. Interestingly we also note an increased probability of collision around the channel centre with the needles. Looking at the absolute relative

velocity $|\boldsymbol{u}_r|$ of collided particle pairs it is clear that the needles and near-spheres differ significantly, as shown in Figure 4. While the mean relative velocity is similar in all regions the PDF for the needles shows much less variation, particularly in the bulk flow region. This could be due to the ability of elongated shapes to align more easily with the local flow and collide more predicably. The same relationship is seen for the relative collision angle (the angle between the velocity vectors of two colliding particles), as shown in Figure 5. Here we again see less variance in PDFs for the needle-like particles indicating that more often these particles collide with velocities nearly parallel, $u_\theta = 0$, and this is likely due to the increased tendency of needle-like particles to algin with the local flow.
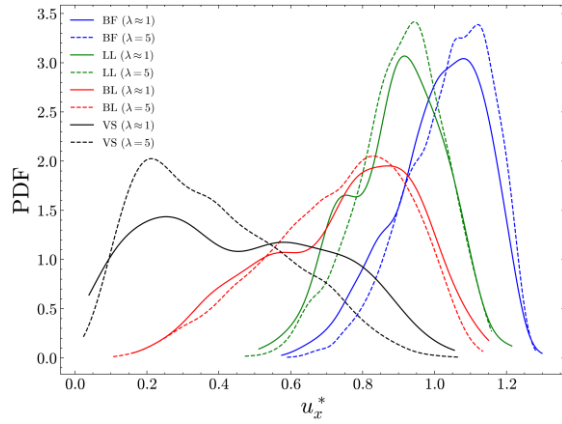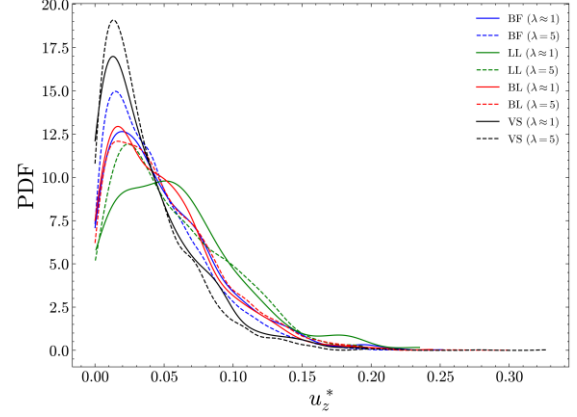

Figure 6: Collided particle streamwise velocity magnitude PDFs separated by flow region
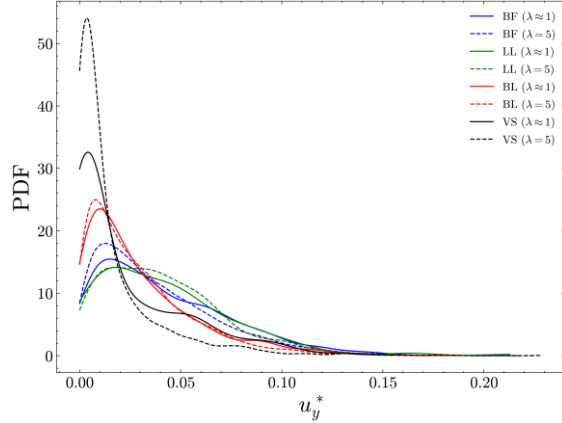
Figure 7: Collided particle wall-normal velocity magnitude PDFs separated by flow region

The mean components of velocity for the nearly spherical particles are in good agreement with the existing literature [5], with similar PDFs observed in all flow regions. The mean streamwise velocity is similar in magnitude between the spherical and needle-like particles, but we do note slightly higher speeds for the needle-like particles in the bulk flow and log-law regions, as shown in Figure 6.

Figure 8: Collided particle spanwise velocity magnitude PDFs separated by flow region

The mean velocity in the wall-normal direction is again similar between the spheres and needles at $\boldsymbol{u}_y^* \approx \boldsymbol{0}$. Here we again observe that the needles have less variance in their speed (Figure 7.), particularly in the very near wall region where the alignment with the streamwise direction is strong. Here the proximity to the near wall boundary layer combined with the particles' tendency to align with the flow, lead to the angle of incidence and thus the lift and drag forces on the needle particles to be quite small. This results in minimal wall-normal velocity fluctuations and the lower variance observed in the PDFs. The mean velocity in the spanwise direction is slightly higher at around $\boldsymbol{u}_z^* \approx \boldsymbol{0}.\boldsymbol{02}$, and this is consistent across both spheres and needles in all the regions considered in Figure 8. Again, we see less variation in the PDFs for needles compared to spheres, but this effect is muted compared to the wall-normal direction with, both particle types performing similarly overall.

4. CONCLUSIONS

Numerical simulations of flows of needle-like and nearly spherical particles under similar conditions have been compared. Our findings indicated that needle-like particles exhibited strong alignment with the streamwise direction near the walls, resulting in higher collision probabilities very close to the walls and around the channel centre. A reduced variance in the relative collision velocity and angles for the needles relative to the spheres was also observed, particularly in the bulk flow region. While the mean velocity components for near-spheres aligned with the existing literature (for perfect spheres), needle-like particles showed slightly higher mean streamwise velocities and less variation in wall-normal and spanwise speeds, especially near the walls due to their strong alignment with the flow. These results underscore the significant impact of particle shape on particle collision behaviour and suggest that further research should be undertaken.

REFERENCES

[1] Allison, M.A., Yuill, B.T., Meselhe, E.A., Marsh, J.K., Kolker, A.S., and Ameen, A.D., 2017, "Observational and Numerical Particle Tracking to Examine Sediment Dynamics in a Mississippi River Delta Diversion", *Estuar Coast Shelf Sci*, Vol. 194, pp. 97-108.

[2] Trojanowicz, M., Kołacińska, K., and Grate, J.W., 2018, "A Review of Flow Analysis Methods for Determination of Radionuclides in Nuclear Wastes and Nuclear Reactor Coolants", *Talanta*, Vol. 183, pp. 70-82.

[3] Lundell, F., Söderberg, L.D., and Alfredsson, P.H., 2011, "Fluid Mechanics of Papermaking", *Annu Rev Fluid Mech*, Vol. 43, pp. 195-217.

[4] Kunnen, R.P.J., Siewert, C., Meinke, M., Schröder, W., and Beheng, K.D., 2013, "Numerically Determined Geometric Collision Kernels in Spatially Evolving Isotropic Turbulence Relevant for Droplets in Clouds", *Atmos Res*, Vol. 127, pp. 8-21.

[5] Rupp, D.A., Mortimer, L.F., and Fairweather, M., 2023, "Stokes Number and Coupling Effects on Particle Interaction Behavior in Turbulent Channel Flows", *Phys Fluids*, Vol. 35, 113307.

[6] Elghobashi, S., 2019, "Direct Numerical Simulation of Turbulent Flows Laden with Droplets or Bubbles", *Annu Rev Fluid Mech*, Vol. 51, pp. 217-244.

[7] Fessler, J.R., Kulick, J.D., and Eaton, J.K., 1994, "Preferential Concentration of Heavy Particles in a Turbulent Channel Flow", *Phys Fluids*, Vol. 6, pp. 3742-3749.

[8] Marchioli, C., and Soldati, A., 2002, "Mechanisms for Particle Transfer and Segregation in a Turbulent Boundary Layer", *J Fluid Mech*, Vol. 468, pp. 283-315.

[9] Mortimer, L.F., Njobuenwu, D.O., and Fairweather, M., 2019, "Near-wall Dynamics of Inertial Particles in Dilute Turbulent Channel Flows", *Phys Fluids*, Vol, 31, 063302.

[10] Marchioli, C., Fantoni, M., and Soldati, A., 2010, "Orientation, Distribution, and Deposition of Elongated, Inertial Fibers in Turbulent Channel Flow", *Phys Fluids*, Vol. 22, 033301.

[11] Eaton, J.K., 2009, "Two-way Coupled Turbulence Simulations of Gas-particle Flows Using Point-particle Tracking", *Int J Multiph Flow*, Vol. 35, pp. 792-800.

[12] Ireland, P.J., Bragg, A.D., and Collins, L.R., 2016, "The Effect of Reynolds Number on Inertial Particle Dynamics in Isotropic Turbulence. Part 1. Simulations Without Gravitational Effects", *J Fluid Mech*, Vol. 796, pp. 617-658.

[13] Dritselis, C.D., 2016, "Direct Numerical Simulation of Particle-laden Turbulent Channel Flows with Two-and Four-way Coupling Effects: Budgets of Reynolds Stress and Streamwise Enstrophy", *Fluid Dyn Res*, Vol. 48, 015507.

[14] Siewert, C., Kunnen, R.P.J., and Schröder, W., 2014, "Collision Rates of Small Ellipsoids Settling in Turbulence, "*J Fluid Mech*, Vol. 758, pp. 686-701.

[15] Chen, M., Kontomaris, K., and McLaughlin, J.B., 1999, "Direct Numerical Simulation of Droplet Collisions in a Turbulent Channel Flow. Part I Collision Algorithm", *Int J Multiph Flow*, Vol. 24, pp. 1079-1103.

[16] van Wachem, B., Zastawny, M., Zhao, F., and Mallouppas, G., 2015, "Modelling of Gas-solid Turbulent Channel Flow with Non-spherical Particles with Large Stokes Numbers", *Int J Multiph Flow*, Vol. 68, pp. 80-92.

[17] Fischer, P.F., Lottes, J.W., and Kerkemeier, S.G., 2008, *Nek5000*, Web page http://nek5000.mcs.anl.gov.

[18] Yin, C., Rosendahl, L., Kær, S.K., and Sørensen, H., 2003, "Modelling the Motion of Cylindrical Particles in a Nonuniform Flow", *Chem Eng Sci*, Vol, 58, pp. 3489-3498.

[19] Ganser, G.H., 1993, "A Rational Approach to Drag Prediction of Spherical and Nonspherical Particles", *Powder Technol*, Vol. 77, pp. 143-152.

[20] Fan, F.G., and Ahmadi, G., 1995, "A Sublayer Model for Wall Deposition of Ellipsoidal Particles in Turbulent Streams", *J Aerosol Sci*, Vol. 26, pp. 813-840.

[21] Breuer, M., and Almohammed, N., 2015, "Modeling and Simulation of Particle Agglomeration in Turbulent Flows Using a Hard-sphere Model with Deterministic Collision Detection and Enhanced Structure Models", *Int J Multiph Flow*, Vol. 73, pp. 171-206.